

# RSC Advances

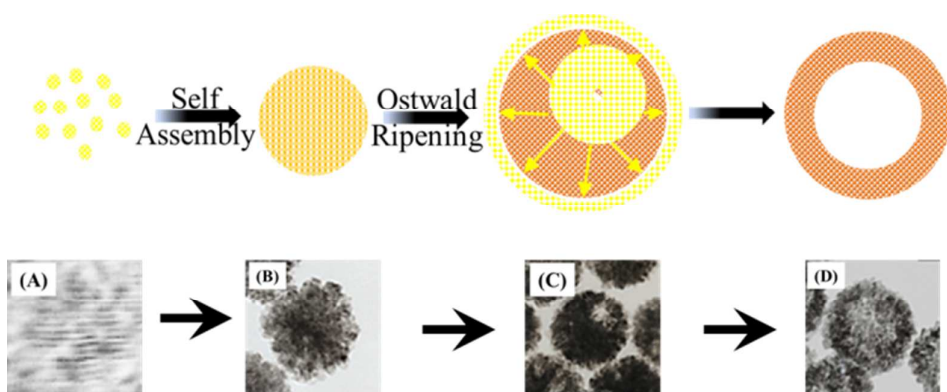


This is an *Accepted Manuscript*, which has been through the Royal Society of Chemistry peer review process and has been accepted for publication.

*Accepted Manuscripts* are published online shortly after acceptance, before technical editing, formatting and proof reading. Using this free service, authors can make their results available to the community, in citable form, before we publish the edited article. This *Accepted Manuscript* will be replaced by the edited, formatted and paginated article as soon as this is available.

You can find more information about *Accepted Manuscripts* in the [Information for Authors](#).

Please note that technical editing may introduce minor changes to the text and/or graphics, which may alter content. The journal's standard [Terms & Conditions](#) and the [Ethical guidelines](#) still apply. In no event shall the Royal Society of Chemistry be held responsible for any errors or omissions in this *Accepted Manuscript* or any consequences arising from the use of any information it contains.



## Porous Cerium Dioxide Hollow Spheres and their Photocatalytic Performance

Saisai Yuan<sup>a,b</sup>, Qitao Zhang<sup>a,b</sup>, Bin Xu<sup>a,b,c</sup>, Zhengyuan Jin<sup>a</sup>, Ya Zhang<sup>e</sup>, Yin Yang<sup>a</sup>, Ming Zhang<sup>b,c,\*</sup>, Teruhisa Ohno<sup>a,d,\*\*</sup>

<sup>a</sup> Department of Applied Chemistry, Faculty of Engineering, Kyushu Institute of Technology, Kitakyushu 804-8550, Japan

<sup>b</sup> School of Chemistry and Chemical Engineering, Yangzhou University, Yangzhou 225002, China

<sup>c</sup> Test Center, Yangzhou University, Yangzhou 225002, China

<sup>d</sup> JST, PRESTO and ACT-C, 4-1-8 Honcho Kawaguchi, Saitama 332-0012, Japan

<sup>e</sup> School of Environmental Science and Engineering, Yangzhou University, Yangzhou 225002, China

**Abstract:** Uniform-sized and monodisperse cerium dioxide porous hollow spheres (CeO<sub>2</sub>-PH) based on the Ostwald ripening process were fabricated by a simple solvothermal method in the absence of any templates. The structure and morphology of CeO<sub>2</sub>-PH and CeO<sub>2</sub>-NP (cerium dioxide nanoparticles) were characterized by X-ray diffraction (XRD), transmission electron microscopy (TEM), field emission scanning electron microscopy (FESEM), and Brunauer-Emmett-Teller (BET) surface area analysis. The average diameter of face-centered cubic (fcc) phase CeO<sub>2</sub>-PH was *ca.* 160 nm with a high specific surface area, and it is composed of small crystal grain particles (*ca.* 10 nm). Furthermore, CeO<sub>2</sub>-PH has high activity for the evaluation of acetaldehyde decomposition. Optical, defect, and chemical state properties were characterized by Raman spectra, ultraviolet-visible absorption spectroscopy (UV-vis), and X-ray photoelectron spectroscopy (XPS). The presence of Ce<sup>3+</sup> ions narrowed the band gap of CeO<sub>2</sub>-PH, resulting in the high light harvesting. The large amount of oxygen vacancy defects provided many activity sites of CeO<sub>2</sub>-PH in the photocatalytic process. The formation scheme and photocatalytic mechanism would be discussed in this paper.

### Introduction

Nanomaterials with a hollow structure have attracted considerable interest in the past few decades due to their low density, high surface area, and wide range of applications in areas such as catalysis, drug delivery, and gas storage.<sup>[1, 2, 3, 4]</sup> Recent developments in the synthesis of particles with a hollow structure have enabled their properties including their mechanical, optical, electrical and chemical properties to be tuned to some degree. For instance, Ma *et al.* have recently modified a previously reported method for Si nanoparticle synthesis to prepare nest-like Si hollow nanospheres with great improvements in cycle life and rate capability.<sup>[5]</sup>  $\alpha$ -Fe<sub>2</sub>O<sub>3</sub> hollow nanospheres, for example, have been shown to have improved photocatalytic performance over  $\alpha$ -Fe<sub>2</sub>O<sub>3</sub> nanocrystals in oxidation of salicylic acid.<sup>[6]</sup> Hollow materials with a porous structure have received much more attention because of their novel properties and potential applications. A porous-hollow structure has a larger surface area, and strong adsorption capacity. This special structure may provide new options for the removal of organic pollutants from waste water.<sup>[7]</sup>

Cerium oxide is one of the most important earth metal oxides, which has been extensively used in various applications including applications in UV blockers, polishing materials, catalysts, electrolytes, sensors, and solar cells due to its favorable properties including

chemical stability, redox property, and high oxygen storage capacity.<sup>[2,8,9]</sup> Notably, ceria is a vital component in three-way catalysts (TWCs) mainly due to its high degree of tolerance to reversible oxygenation-deoxygenation cycles without disruption of fluorite lattice structure.<sup>[10-12]</sup> In the past few decades, various morphologies of ceria including cubes, octahedra, spheres, wires and rods have been investigated. Very recently, ceria with hollow a structure has been fabricated by various methods.<sup>[13-16]</sup> Thin layers (*ca.* 12 nm) of cerium oxide were deposited onto *ca.* 200-nm-thick silica colloid templates using cerium nitrate and the silica cores were subsequently removed to yield hollow spheres.<sup>[17]</sup> Novel single-crystalline-like CeO<sub>2</sub> hollow nanocubes were synthesized through a solvothermal method using peroxyacetic acid (PAA) as the oxidant in the absence of a template. Solid evacuation in the central part via Ostwald ripening led to the formation of single-crystalline-like hollow nanocubes.<sup>[18]</sup> Liang *et al.* synthesized CeO<sub>2</sub>-ZrO<sub>2</sub> solid solution nanocages with

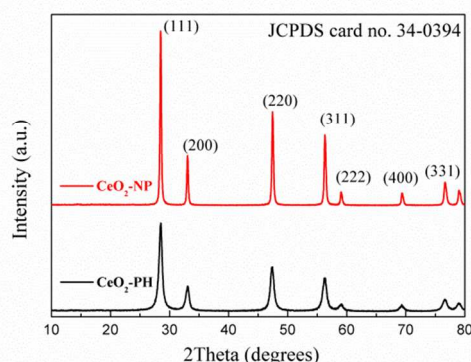


**Fig 1.** XRD patterns of the CeO<sub>2</sub> nanoparticles (CeO<sub>2</sub>-NP), and the CeO<sub>2</sub> porous-hollow spheres (CeO<sub>2</sub>-PH).

\* Corresponding author at: School of Chemistry and Chemical Engineering, Yangzhou University, Yangzhou 225002, China. Tel.: +86 51487990926; fax: +86 51487979244.

\*\* Corresponding author at: Department of Applied Chemistry, Faculty of Engineering, Kyushu Institute of Technology, Kitakyushu 804-8550, Japan. Tel.: +81 93 884 3318; fax: +81 93 884 3318.

E-mail addresses: lxyzhangm@yzu.edu.cn (M. Zhang), tohno@che.kyutech.ac.jp (T. Ohno)

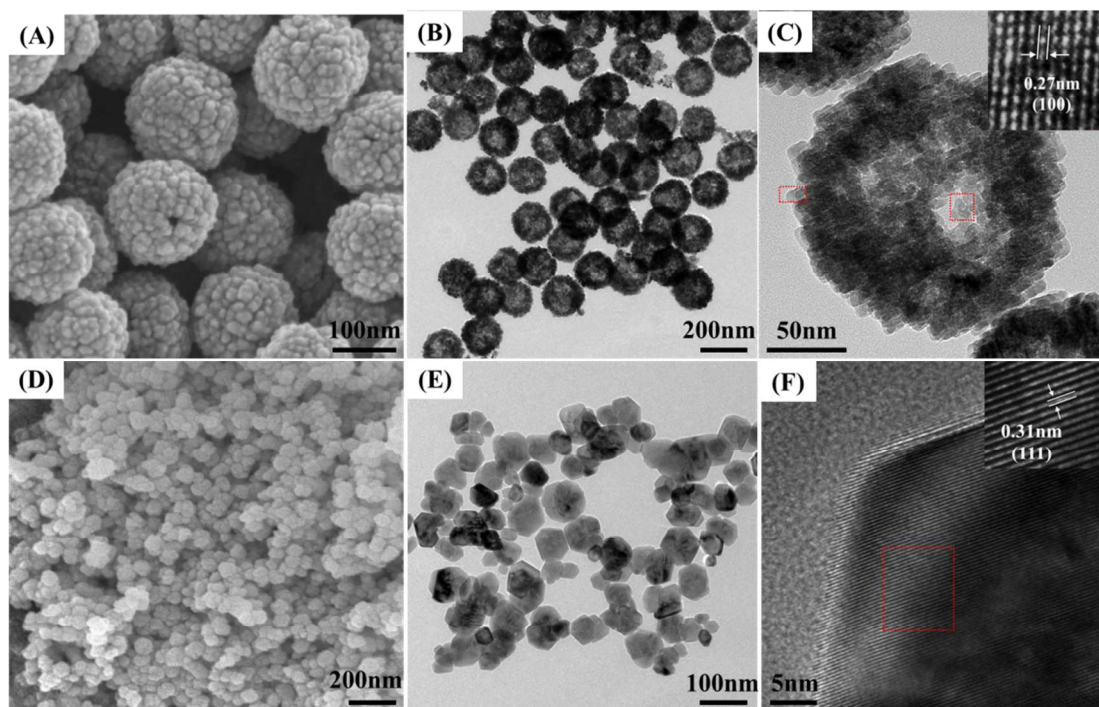
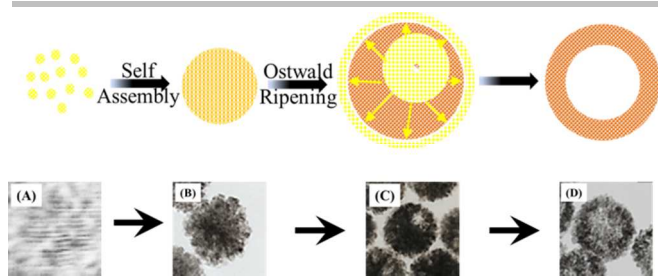


**Fig 2.** SEM images of (A) the CeO<sub>2</sub> hollow spheres, (D) the CeO<sub>2</sub> nanoparticles; TEM images of (B) & (C) the CeO<sub>2</sub> hollow spheres, (E) & (F) the CeO<sub>2</sub> nanoparticles, the inset is the HRTEM images.

controllable structures via the Kirkendall effect.<sup>[19]</sup> Different morphologies would have various application, especially, the hollow structure was favourable for the catalysis.

Literature reported some special morphologies of ceria, which were applied to the photocatalysis.<sup>[20, 21]</sup> In this work, ceria porous-hollow spheres were synthesized by a simple solvothermal method in the absence of any templates via Ostwald ripening. The morphology, structure and other properties were characterized by TEM, FESEM, BET, XRD, Raman, UV-vis, and XPS, and the photocatalytic performance was evaluated by degradation of acetaldehyde. Compared with the previous reports, the synthetic process was one-step and very simple, simultaneously, the special porous hollow spheres structure was applied to the degradation of acetaldehyde, which had many potential applications.



Schem1 formation of the porous-hollow structure; (A), (B), (C), (D) are corresponding to the Fig S 1.

## Experimental Section

All chemicals used in the experimental section were analytical grade and used as received without further purification.

**Photocatalyst preparation.** CeO<sub>2</sub> hollow spheres with ~140 nm in diameters were synthesized by a simple one-step template-free solvothermal method with reaction in a mixed solution of water, ethanol and glycol together with PVP (polyvinyl pyrrolidone) as a surfactant. Typically, 1.0 g of Cerium(III) nitrate hexahydrate and 0.10 g of PVP were dissolved in a mixture of EG (20 mL), EtOH (40 mL) and H<sub>2</sub>O (20 mL) with magnetic stirring for 3 h. Then the suspension was transferred to a 100-mL Teflon-lined autoclave and heated at 180 °C for 24 h. After cooling to room temperature, the product was

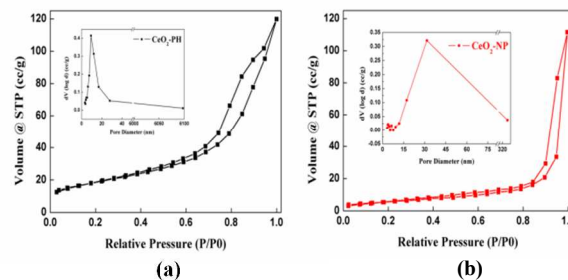


**Fig 3.** N<sub>2</sub> adsorption-desorption isotherm, and *inset* is the corresponding BJH pore size distribution curves, (a) the ceria porous-hollow spheres, (b) the ceria nanoparticles.

**Table 1. Summary of the XRD and BET calculation results**

Type	Average Primary Particle size (Å)	S <sub>BET</sub> (m <sup>2</sup> /g)	Pore Size Distribution (nm)/Type	Pore Volume (cc/g)
CeO <sub>2</sub> -PH	103	65.91	3 ~30 / mesoporous	0.181
CeO <sub>2</sub> -NP	298	20.08	10 ~350 / macroporous	0.173

collected by centrifugation, washed with ethyl alcohol and water until the ionic strength was less than 10 μs/cm, and dried at 70 °C overnight. Finally, we obtained hollow-sphere cerium dioxide, which was denoted as CeO<sub>2</sub>-PH.

For control experiments, ceria nanoparticles were obtained under same conditions as those described above but in the absence of glycol, and the nanoparticles were denoted as CeO<sub>2</sub>-NP.

**Characterization.** The CeO<sub>2</sub> materials were characterized using X-ray diffraction (XRD), X-ray photoelectron spectroscopy (XPS), field emission scanning electron microscopy (FESEM), transmission electron microscopy (TEM), high-resolution (HRTEM), ultraviolet-visible absorption spectroscopy (UV-vis), Brunauer-Emmett-Teller (BET) surface area analysis and Raman spectra.

The crystal structure and composition were determined by XRD using a Rigaku MiniFlex II X-ray diffractometer with a Cu-Kα radiation source ( $\gamma = 1.5405\text{Å}$ ). The morphologies of the samples were observed by FESEM (JEOL, JSM-6701FONO) and TEM (Hitachi, H-9000NAR, 200 kV). HRTEM analysis was conducted using a Tecnai G2 F30 S-TWIN (300 kV). Nitrogen adsorption/desorption measurements were performed at 77 K using a Quantachrome Nova 4200e to calculate the specific surface area using the BET model. The pore size distribution was obtained from desorption-isotherm curves by the Barrett Joyner Halenda (BJH) method. Prior to measurements, the samples were degassed in vacuum at 180 °C for 3 h. Diffuse reflectance (DR) spectra were measured using a UV-vis spectrophotometer (Shimadzu, UV-2500PC) equipped with an integrating sphere unit (Shimadzu, ISR-240A). Raman spectra were obtained by a laser Raman spectrum (JASCO, NRS-5100). An XPS experiment was carried on a Thermo ESCALAB 250Xi system at room temperature under Al Kα using monochromatic radiation and C1s peak ( $284.70 \pm 0.1$  eV) reference. The background of XPS spectra was subtracted by the Shirley procedure and the peaks were fitted using the Gaussian-Lorentzian function.

**Photocatalytic activity test.** Photocatalytic activity of the samples was evaluated by photocatalytic decomposition of acetaldehyde in gas phase. Samples powder (150 mg), which had completed extinction of incident radiation, was spread on a glass dish, and the glass dish was put into a Tedlar bag (AS ONE Co. Ltd.) with a volume of 125 mL mixed air (79% N<sub>2</sub>, 21% O<sub>2</sub>,

<0.1 ppm of CO<sub>2</sub>, 500 ppm of acetaldehyde). After 2-h adsorption equilibrium in the dark, the photocatalysts were exposed under the visible light. A light-emitting diode (LED; Lumileds, Luxeon LXHL-NRR8), which emitted light at a wavelength of *ca.* 435 nm with an intensity of 3.0 mW cm<sup>-2</sup>, was used as visible-light irradiation source. In the photocatalysis process, generation of carbon dioxide and consumption of acetaldehyde were monitored by online gas chromatography (Agilent Technologies, 3000A Micro-GC, TCD detector) equipped with OV1 and PLOT-Q columns.

### Results and discussion

The phase purity of the prepared products was estimated by the XRD patterns. *Fig. 1* Shows the XRD patterns of CeO<sub>2</sub>-NP and CeO<sub>2</sub>-PH. All of the characteristic peaks were indexed to the face-centered cubic phase with space group *Fm* $\bar{3}$ *m* of ceria (JCPDS card no. 34-0394). No other peaks were detected, and the sharp peaks indicated that the high purity and the highly crystalline nature of both samples. Compared with the CeO<sub>2</sub>-NP, the peaks of CeO<sub>2</sub>-PH were relatively broad, demonstrating that the CeO<sub>2</sub>-PH was composed of smaller crystals. The average primary particle size was *ca.* 10 nm (*Table 1*), which is according to the calculation with the Debye-Scherrer formula for the strongest peak (111).

The morphologies of the as-prepared CeO<sub>2</sub> photocatalysts were shown in *Fig. 2*. *Fig. 2A* shown an SEM image of ceria hollow spheres, which were composed of small nanoparticles. The diameter of the ceria hollow spheres was *ca.* 160 nm, and the particle size of the small nanoparticles was *ca.* 10 nm, which was in accordance with the XRD calculation (*Fig. 1*). The voids that can be seen in *Fig. 2A* suggested that the obtained ceria are porous-hollow spheres. TEM and HRTEM were performed to obtain more information about the special morphology. The low TEM image in *Fig. 2B* clearly shown a hollow structure of the prepared sample. It had a narrow size distribution and the diameter was in

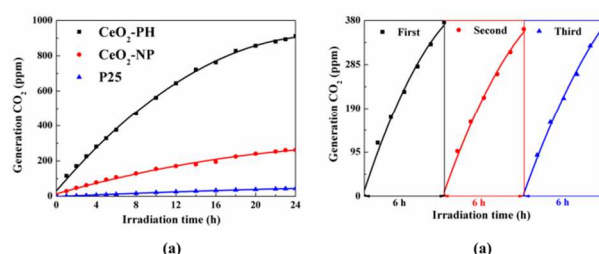


**Fig 4.** (a) Time courses of CO<sub>2</sub> evolution from acetaldehyde decomposition over the products under visible-light irradiation, (b) cycling performance of CeO<sub>2</sub>-PH.

accordance with the SEM observation. In the amplified TEM image shown in *Fig. 2C*, the contrast between the dark margins and the pale center confirmed the existence of a hollow structure. Moreover, it revealed that the hollow ceria spheres consisted of small nanoparticles with a porous structure. This special morphology with a high specific surface area would be favorable for a photocatalysis process due to the full access of reactants (acetaldehyde in this study). The structure of the as-obtained ceria porous-hollow sphere nanocrystals was investigated in more detail by HRTEM (*Fig. 2C inset*). The spacing of the measured 2D lattice fringes was close to 0.27 nm indexed to the interplanar spacing of the (100) plane of the outside and inside surfaces.<sup>[22, 23, 24]</sup> To understand the formation mechanism of the porous-hollow structure, samples synthesized with different reaction times were collected and analyzed. A plausible formation scheme of the hollow CeO<sub>2</sub> sphere is illustrated in *Scheme 1*. When PVP and Ce(NO<sub>3</sub>)<sub>3</sub>·6H<sub>2</sub>O are dissolved in an aqueous ethanol and EG solution resulting in a homogeneous mixture, cerium ions are well surrounded by PVP molecules due to the strong interaction between the nuclei and surfactant. Nanoparticles followed by self-assembling of ceria nanoparticles to form a sphere shape because of the isotropic growth. The hollow shape is formed because cerium nanoparticles tend to move towards the wall of the sphere due to the density variation among nanoparticles and then undergo the Ostwald ripening process.<sup>[25,7,26]</sup> Due to the difference of surface energy and particles located in the inner space of the spheres and this particles could be dissolved and merged by particles in the outer surface, and meanwhile the solid sphere gradually develops into a hollow structures. The factors of the porous-hollow structure formation will be presented in supporting information (*Fig. S1*). *Fig. 2(D) ~ (F)* show SEM, TEM, and HRTEM images of the ceria nanoparticles, which was set as the contrast samples. The

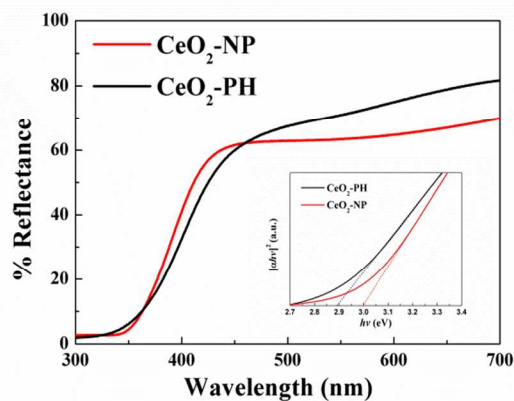


Fig 5. UV-vis diffuse reflectance spectra of CeO<sub>2</sub>-NP and CeO<sub>2</sub>-PH; the inset is the  $(\alpha hv)^2$  versus  $hv$  plots curves.

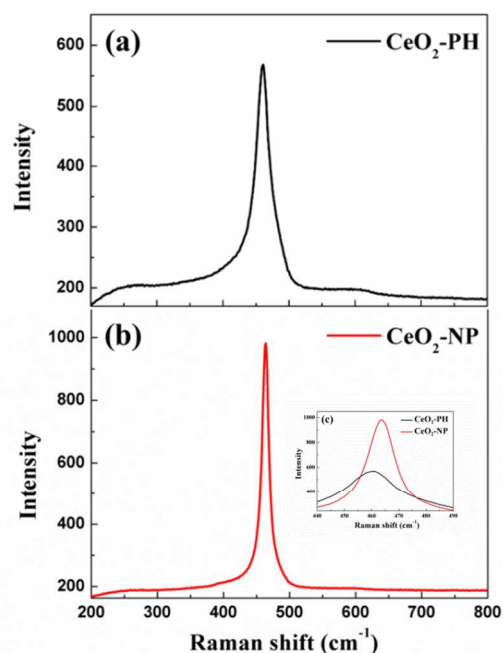


Fig 6. Raman spectra of samples (a) the CeO<sub>2</sub>-PH, (b) the CeO<sub>2</sub>-NP, (c) enlarged image on dominant peak of both CeO<sub>2</sub>-PH and CeO<sub>2</sub>-NP.

sizes of nanoparticles were about 50 nm ~ 100 nm, and slight agglomeration can be seen in the SEM image in *Fig. 2D* of the SEM image. Compared to previously prepared ceria, these ceria nanoparticles had better crystallinity as shown in the HRTEM image in *Fig. 2F*, though the dispersibility was not so good due to the absence of glycol. Glycol possesses a capping reagent function, and it also has a possibility of dissolution of the metal salt. The lattice fringe in the HRTEM image (*Fig. 2F inset*) show a spacing of 0.31 nm from the (111) plane of the cubic ceria.<sup>[22]</sup>

Furthermore, the N<sub>2</sub> adsorption-desorption isotherms and pore size distribution of CeO<sub>2</sub>-PH and CeO<sub>2</sub>-NP are shown in *Fig. 3*. The shape of the isotherm (*Fig. 3a*) with a hysteresis loop ranging from 0.4 to 1.0 in the relative pressure corresponds to a type-IV isotherm according to the Brunauer-Deming-Deming-Teller (BDDT) classification, simultaneously revealing the existence of a mesoporous structure in CeO<sub>2</sub>-PH. *Fig. 3b* (CeO<sub>2</sub>-NP) exhibits the type-III isotherms with hysteresis loops at the relative pressures of 0.8 ~ 1.0, indicating the presence of disordered macroporous structure.<sup>[27]</sup> The pore size distribution of CeO<sub>2</sub>-PH (*Fig. 3a inset*) was determined by the Barrett-Joyner-Halenda (BJH) method from the desorption branch of the isotherm. The pore size distribution is narrow, from 3 nm to 30 nm, in the mesoporous region, centered at 9 nm, and the pore volume is 0.181 cc/g, which is attributed to the aggregation of small crystal particles. However, CeO<sub>2</sub>-NP (*Fig. 3b inset*) has a broad pore size distribution ranging

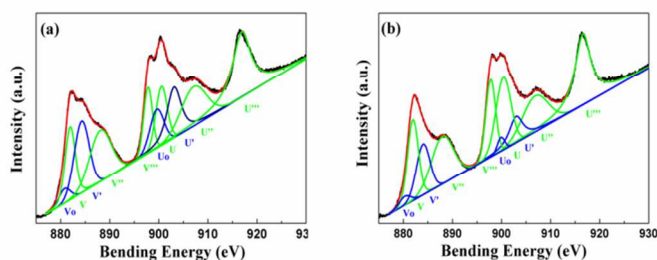


Fig 7. Ce 3d spectra (a) the CeO<sub>2</sub>-PH, (b) the CeO<sub>2</sub>-NP.

from 10 nm to 350 nm and the pore volume is 0.173 cc/g, which is attributed to the void spaces among the stacked ceria nanoparticles. The specific surface areas of the CeO<sub>2</sub>-PH and CeO<sub>2</sub>-NP were 65.91 m<sup>2</sup>/g, and 20.08 m<sup>2</sup>/g respectively, which were calculated by the Brunauer-Emmett-Teller (BET) equation (Table 1).

Table 1 is a summary of the results of XRD and BET calculations results. Compared with CeO<sub>2</sub>-NP, CeO<sub>2</sub>-NP has a small average primary particle size, high specific surface area, narrow pore size distribution and large pore volume, which are attributed to the smaller crystal size and the special porous-hollow sphere structure. These excellent properties will be favourable for a photocatalysis process.

**Photocatalytic activity study.** The photocatalytic activity of CeO<sub>2</sub>-PH was examined in acetaldehyde decomposition reaction under visible light irradiation, and the activity of CeO<sub>2</sub>-NP and P25 were also estimated in the same condition for comparison. Fig. 4a shows the CO<sub>2</sub> evaluation activities of CeO<sub>2</sub>-NP, CeO<sub>2</sub>-PH and P25. After 24-h visible light irradiation, the degradation efficiencies of P25, CeO<sub>2</sub>-NP and CeO<sub>2</sub>-PH were ca. 5%, 25% and 92%, respectively. The activity of CeO<sub>2</sub>-PH sample was about 4-times higher than the contrast sample for CeO<sub>2</sub>-NP, and the 18-times higher than the P25 (P25 has no response to the visible light). One plausible reason of the higher activity is the larger S<sub>BET</sub> of CeO<sub>2</sub>-PH. Compared with CeO<sub>2</sub>-NP the porous and hollow structure was the predominant reason for the higher S<sub>BET</sub>, which provided superior adsorption and reactive sites for decomposition of acetaldehyde. However, the primary particle size (ca. 10 nm) of the CeO<sub>2</sub>-PH was smaller than that of CeO<sub>2</sub>-NP (50 nm ~ 100 nm), as observed in FESEM images. The presence of quantum effects has a great influence on properties of the surfaces of samples, such as electrical and optical performances. These special properties play the critical roles in the photocatalysis process, which can be as another more important credible reason for the excellent photocatalytic performance. The surface property and mechanism are discussed in detail in the following section. In order to estimate the stability of the CeO<sub>2</sub>-PH, cycling performance was tested. The result was shown in Fig. 4b. After 6 h irradiation, the generation

of CO<sub>2</sub> were 376.226 ppm (first), 361.593 ppm (second) and 370.159 ppm (third), which indicated that the stability of photocatalyst (CeO<sub>2</sub>-PH) was excellent.

For ultraviolet-blocking materials, ceria has a strong absorption in the ultraviolet range. Fig. 5 shows UV-vis diffuse reflectance spectra of CeO<sub>2</sub>-NP and CeO<sub>2</sub>-PH. There is a strong absorption band from 300 nm to 350 nm in the spectra, which is assigned to the charge transfer from O<sup>2-</sup> in O 2p to Ce<sup>4+</sup> in Ce 4f. The prepared CeO<sub>2</sub>-PH had fractional absorption in the visible region. As semiconductor materials, the direct band gap (*E<sub>g</sub>*) can be calculated from the equation of  $ahv = A(hv - E_g)$ , where *hν* is the photon energy, *α* is the absorption coefficient, and *A* is a constant of CeO<sub>2</sub>.<sup>[28]</sup> Calculated *E<sub>g</sub>* values for CeO<sub>2</sub>-NP and CeO<sub>2</sub>-PH were 2.88 eV and 3.01 eV, respectively (Fig. 5 inset), which are smaller than the theoretical value of 3.2 eV for bulk CeO<sub>2</sub>. There are two plausible theories for the expiation of the final moderate red-shift of the CeO<sub>2</sub>-PH. The existence of quantum confinement effect due to the nanoscale size of the primary particles forming the porous-hollow spheres resulted in a blue-shift in the UV-vis diffuse reflectance spectrum. Simultaneously, the decrease in primary particle size led to an increase in the Ce<sup>3+</sup> ion concentration<sup>[29]</sup> (XPS results in Fig. 7). Chen *et al.* found out that the blue-shift of the absorption edge in a CeO<sub>2</sub> film occurred with a decrease in the Ce<sup>3+</sup> content.<sup>[30, 31]</sup> Therefore, the red-shift of the band gap for CeO<sub>2</sub>-PH should originate from the transformation between Ce<sup>4+</sup> to Ce<sup>3+</sup>.<sup>[32]</sup> In conclusion, band gap narrowing is the integrated result of the two mentioned reasons, which is beneficial for the photocatalytic process.

The visible Raman spectra (Fig. 6) are dominated by a strong F<sub>2g</sub> symmetry mode of CeO<sub>2</sub> fluorite phase at 464 cm<sup>-1</sup> on CeO<sub>2</sub> with weak bands at 258 cm<sup>-1</sup> and 595 cm<sup>-1</sup>, due to second-order transverse acoustic (2TA) mode and defect-induced (D), respectively. The slight shift to 461 cm<sup>-1</sup> (Fig. 6c inset) and the obvious lower intensity of this mode implied that CeO<sub>2</sub>-PH had a stronger the symmetry of Ce—O bond also led to a stronger optical absorption as different colors on these samples (grey on CeO<sub>2</sub>-NP and yellow on CeO<sub>2</sub>-PH, in accordance with the UV-vis test).<sup>[33]</sup> The ionic radii of Ce<sup>3+</sup> and Ce<sup>4+</sup> are 1.034 Å and 0.92 Å, respectively. When Ce<sup>3+</sup> (Fig. 7 XPS results) was induced Ce—O bond, the lattice constant increased, sequentially, slight red-shift occurred.<sup>[34, 35]</sup> Compared with CeO<sub>2</sub>-NP (Fig. 6b), CeO<sub>2</sub>-PH (Fig. 6a) shown a stronger intensity in ca. 595 cm<sup>-1</sup> (D), indicating that CeO<sub>2</sub>-PH had much more intrinsic defects. The relative intensity ratios of I<sub>D</sub>/I<sub>F<sub>2g</sub></sub> were calculated to be about 1.8% (CeO<sub>2</sub>-PH) and 0.5% (CeO<sub>2</sub>-NP). It has been proved that the presence of surface defects, such as large size oxygen vacancy clusters,<sup>[36]</sup> would promote the transformation of Ce<sup>4+</sup> to Ce<sup>3+</sup> for CeO<sub>2</sub>-based materials.

In order to investigate in more detail the surface

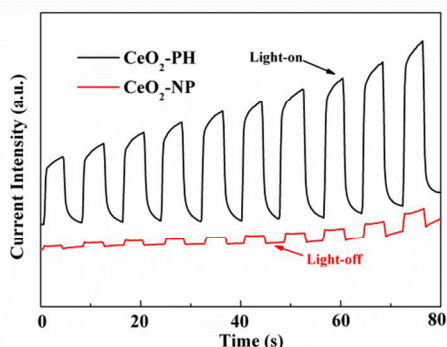


Fig 8. Photocurrent response of the photoanodes to light on-off collected from CeO<sub>2</sub>-NP and CeO<sub>2</sub>-PH electrodes in the solution of 1.0 M Na<sub>2</sub>SO<sub>4</sub> under light illumination.

composition and chemical state, XPS analysis was carried out. The CeO<sub>2</sub> spectrum is composed of two multiplets (*v* and *u*), which correspond to the spin-orbit split 3d<sub>5/2</sub> and 3d<sub>3/2</sub> core holes. Fig. 7 shows the Ce 3d<sub>3/2</sub> and Ce 3d<sub>5/2</sub> spectra of the CeO<sub>2</sub>-PH (a) and CeO<sub>2</sub>-NP (b), respectively. The spectra of Ce 3d can be decomposed into ten peaks by Gaussian-Lorentzian function fitting. According to previous research, the labels *u*, *u*'', *u*'',', *v*, *v*' and *v*'',', refer to Ce 3d<sub>3/2</sub> and Ce 3d<sub>5/2</sub> are characteristic peaks of Ce<sup>4+</sup> in CeO<sub>2</sub>. The highest binding energy (BE) peaks *U*'',', and *V*'',', are located at 916.9 eV and 898.2 eV and arise from the Ce (3d<sup>9</sup>4f<sup>0</sup>) O (2p<sup>6</sup>) final state. The lower BE states *U*'',', and *V*'',', are located at 907.5 eV and 888.95 eV and are assigned to Ce (3d<sup>9</sup>4f<sup>1</sup>) O (2p<sup>5</sup>). The BE peaks of *U* and *V* at 901.1 eV and 881.89 eV are attributed to the Ce (3d<sup>9</sup>4f<sup>2</sup>) O (2p<sup>4</sup>) final state. In case of Ce 3d of Ce<sup>3+</sup>, BE peaks of Ce 3d consist of two pairs of doublets (*U*<sub>0</sub>, *V*<sub>0</sub>, *U*' and *V*'). For Ce<sup>3+</sup>, the highest BE peaks *U*' and *V*' appear at 903.4 eV and 885.02 eV, respectively. These doublets correspond to Ce (3d<sup>9</sup>4f<sup>1</sup>) O (2p<sup>5</sup>). The lowest BE peaks *U*<sub>0</sub> and *V*<sub>0</sub> appear at 880.2 eV and 898.2 eV and correspond to Ce (3d<sup>9</sup>4f<sup>1</sup>) O (2p<sup>6</sup>)<sup>[37]</sup>. It can be seen that the chemical valence of cerium on the surface of the samples was a mixed valence state, and was mainly Ce<sup>4+</sup> plus a small fraction of Ce<sup>3+</sup>. The semi-quantified calculations of the amount of Ce<sup>3+</sup> were following the equation  $Ce^{3+} = [Av_0 + Av' + Au_0 + Au'] / [Av_0 + Av + Av' + Av'' + Av''' + Au_0 + Au + Au' + Au'' + Au''']$ , and the values were 30.1% (CeO<sub>2</sub>-PH) and 17.6% (CeO<sub>2</sub>-NP), respectively. The high content of Ce<sup>3+</sup> in CeO<sub>2</sub>-PH was ascribed to the solvent (ethylene glycol), smaller primary particle size,<sup>[29]</sup> and more oxygen vacancy defects. Ethylene glycol has reducibility and Ce<sup>4+</sup> can be converted into Ce<sup>3+</sup> in the reaction process. In the case of more oxygen vacancy defects, proved in Raman spectra (Fig 6), more oxygen vacancy defects facilitated more amount of Ce<sup>3+</sup>. The reason why CeO<sub>2</sub>-PH (100) can generate a large amount of Ce<sup>3+</sup> compared with CeO<sub>2</sub>-NP (111) is associated with the exposed crystal planes. The

oxygen vacancy formation energy, nature and amount of the defects and low coordination sites are intrinsically affected by the surface planes of the ceria nanoshapes. Based on density functional theory calculations, the stability follows the sequence (111) > (110) > (100), while the activity follows the opposite order. The energy required to form oxygen vacancies on the (100) surface is less than those on the (111) and (110) surfaces due to its intrinsic high energy.

**Photoelectrochemical response.** In order to further account for the high activity of CeO<sub>2</sub>-PH, its photoelectrochemical response has been measured.<sup>[38,39,40]</sup> The photoelectrochemical properties of the two types of CeO<sub>2</sub> were characterized by measuring the photocurrent under a 500 W Xe lamp equipped with a cutoff filter ( $\lambda > 325$  nm), and the initial and final potential were 0 V and 0.4 V, respectively. Fig. 8 shows the photocurrent responses of the photoanodes prepared from CeO<sub>2</sub>-PH and CeO<sub>2</sub>-NP. As anticipated, CeO<sub>2</sub>-PH exhibited an excellent photoelectrochemical response, being about 5-times higher than that of CeO<sub>2</sub>-NP. The enhancement of the photocurrent for CeO<sub>2</sub>-PH can be attributed to the improvement of light-harvesting, as shown in the result for band gap value. In addition, the high content of Ce<sup>3+</sup> ions would be trapped by the photogeneration holes<sup>[32]</sup>, and then facilitated the separation of the photogeneration electron-hole pairs. The trapped holes would restrain the recombination of the photogeneration electron-hole, and then enhanced the photocurrent response. As a result, CeO<sub>2</sub>-PH (higher Ce<sup>3+</sup> ion content) has a stronger photoelectrochemical response, which is in accordance with activity in the evaluation of acetaldehyde degradation. Moreover, the defects, shown in Raman and XPS characterizations, in CeO<sub>2</sub>-PH might lead to the formation of a surface state energy band of oxygen and the oxygen adsorption, desorption and diffusion processes would easily occur on the surface, resulting in notable changes in the properties of CeO<sub>2</sub>-PH such as optical and electrical properties.<sup>[41]</sup> When the incident light is larger than the band gap, previously adsorbed oxygen on the surface of the CeO<sub>2</sub>-PH will desorb and release free electrons, causing the conductivity to increase.

## Conclusion

In summary, porous CeO<sub>2</sub> hollow spheres were successfully synthesized by a one-step solvothermal method in the absence of any templates. Based on the morphology evolution of that time-dependent samples (Fig. 5), it is thought that Ostwald ripening occurs and that it is the main driving force for the core evacuation of solid aggregates during the hollowing process. Furthermore, the prepared CeO<sub>2</sub>-PH has high activity for decomposition of the acetaldehyde. The presence of Ce<sup>3+</sup> and oxygen vacancies in CeO<sub>2</sub>-PH enhanced the light harvesting and provided activity sites in the

photocatalytic process. In addition, this prepared special porous-hollow sphere can be used in many potential applications in the future.

**Acknowledgment.** This work was supported by JST PRESTO program and JST ACT-C program. The authors are also grateful for financial support by the National Natural Science Foundation of China (No. 50873085 and No. 21307104).

**Supporting information available:**

## References

1. P. M. Arnal, M. Comotti and F. Schuth, *Angewandte Chemie*, 2006, 45, 8224-8227.
2. L. Liao, H. X. Mai, Q. Yuan, H. B. Lu, J. C. Li, C. Liu, C. H. Yan, Z. X. Shen and T. Yu, *The Journal of Physical Chemistry C*, 2008, 112, 9061-9065.
3. X. Liang, J. J. Xiao, B. H. Chen and Y. D. Li, *Inorganic Chemistry*, 2010, 49, 8188-8190.
4. Y. F. Zhu, J. L. Shi, W. H. Shen, X. P. Dong, J. W. Feng, M. L. Ruan and Y. S. Li, *Angew. Chem.-Int. Edit.*, 2005, 44, 5083-5087.
5. H. Ma, F. Cheng, J. Chen, J. Zhao, C. Li, Z. Tao and J. Liang, *Advanced Materials*, 2007, 19, 4067-4070.
6. B. Xu, B. Huang, H. Cheng, Z. Wang, X. Qin, X. Zhang and Y. Dai, *Chem Commun (Camb)*, 2012, 48, 6529-6531.
7. Z. Yang, J. Wei, H. Yang, L. Liu, H. Liang and Y. Yang, *European Journal of Inorganic Chemistry*, 2010, 2010, 3354-3359.
8. C. Laberty-Robert, J. W. Long, E. M. Lucas, K. A. Pettigrew, R. M. Stroud, M. S. Doescher and D. R. Rolison, *Chemistry of Materials*, 2006, 18, 50-58.
9. D. Zhang, X. Du, L. Shi and R. Gao, *Dalton transactions*, 2012, 41, 14455-14475.
10. D. Gerceker and I. Onal, *Applied Surface Science*, 2013, 285, 927-936.
11. K. Tanimoto, H. Kato, S. Takeshita, M. Hidaka, S. Hinokuma and M. Machida, *Bulletin of the Chemical Society of Japan*, 2013, 86, 1327-1332.
12. Z. Zhan, X. Liu, D. Ma, L. Song, J. Li, H. He and H. Dai, *Frontiers of Environmental Science & Engineering*, 2014, 8, 483-495.
13. C. Ho, J. C. Yu, T. Kwong, A. C. Mak and S. Lai, *Chemistry of Materials*, 2005, 17, 4514-4522.
14. S. W. Yang and L. Gao, *Journal of the American Chemical Society*, 2006, 128, 9330-9331.
15. Q. Wu, F. Zhang, P. Xiao, H. Tao, X. Wang, Z. Hu and Y. Lü, *The Journal of Physical Chemistry C*, 2008, 112, 17076-17080.
16. T. Taniguchi, K.-i. Katsumata, S. Omata, K. Okada and N. Matsushita, *Crystal Growth & Design*, 2011, 11, 3754-3760.
17. N. C. Strandwitz and G. D. Stucky, *Chemistry of Materials*, 2009, 21, 4577-4582.
18. G. Chen, C. Xu, X. Song, S. Xu, Y. Ding, and S. Sun, *Crystal Growth and Design*, 2008, 8, 4449-4453.
19. X. Liang, X. Wang, Y. Zhuang, B. Xu, S. Kuang and Y. Li, *Journal of the American Chemical Society*, 2008, 130, 2736-2737.
20. C. Zhang, X. Zhang, Y. Wang, S. Xie, Y. Liu, X. Lu and Y. Tong, *New Journal of Chemistry*, 2014, 38, 2581-2586.
21. B. Xu, Q. Zhang, S. Yuan, M. Zhang and T. Ohno, *Applied Catalysis B: Environmental*, 2015, 164, 120-127.
22. E. Aneggi, D. Wiater, C. de Leitenburg, J. Llorca and A. Trovarelli, *ACS Catalysis*, 2014, 4, 172-181.
23. Y. Chen, S. Lv, C. Chen, C. Qiu, X. Fan and Z. Wang, *Journal of Physical Chemistry C*, 2014, 118, 4437-4443.
24. P. Zhao, A. Ito and T. Goto, *Ceramics International*, 2014, 40, 605-609.
25. H. C. Zeng, *Current Nanoscience*, 2007, 3, 177-181.
26. F. Z. Guozhu Chen, Xuan Sun, Sixiu Sun and Ruiping Chen, *CrystEngComm*, 2011, 13, 2904-2908.
27. J. C. Groen, L. A. A. Peffer and J. Pérez-Ramírez, *Microporous and Mesoporous Materials*, 2003, 60, 1-17.
28. Z. Wang, Z. Quan and J. Lin, *Inorganic Chemistry*, 2007, 46, 5237-5242.
29. S. Deshpande, S. Patil, S. V. N. T. Kuchibhatla and S. Seal, *Applied Physics Letters*, 2005, 87, 133113.
30. M. Y. Chen, X. T. Zu, X. Xiang and H. L. Zhang, *Physica B: Condensed Matter*, 2007, 389, 263-268.
31. S. Tsunekawa, J.-T. Wang, Y. Kawazoe and A. Kasuya, *Journal of Applied Physics*, 2003, 94, 3654.
32. X. Lu, T. Zhai, H. Cui, J. Shi, S. Xie, Y. Huang, C. Liang and Y. Tong, *Journal of Materials Chemistry*, 2011, 21, 5569.
33. J. Lin, L. Li, Y. Huang, W. Zhang, X. Wang, A. Wang and T. Zhang, *The Journal of Physical Chemistry C*, 2011, 115, 16509-16517.
34. B. Liu, M. Yao, B. Liu, Z. Li, R. Liu, Q. Li, D. Li, B. Zou, T. Cui, G. Zou, J. Liu and Z. Chen, *Journal of Physical Chemistry C*, 2011, 115, 4546-4551.
35. J. E. Spanier, R. D. Robinson, Z. Feng, C. Siu-Wai and I. P. Herman, *Physical Review B (Condensed Matter and Materials Physics)*, 2001, 64, 245407/245401-245408.

36. X. W. Liu, K. B. Zhou, L. Wang, B. Y. Wang and Y. D. Li, *Journal of the American Chemical Society*, 2009, 131, 3140-3141.
37. E. Bêche, P. Charvin, D. Perarnau, S. Abanades and G. Flamant, *Surface and Interface Analysis*, 2008, 40, 264-267.
38. A. Paracchino, V. Laporte, K. Sivula, M. Grätzel and E. Thimsen, *Nature materials*, 2011, 10, 456-461.
39. Y. Liu, S. Xie, C. Liu, J. Li, X. Lu and Y. Tong, *Journal of Power Sources*, 2014, 269, 98-103.
40. G. L. Wang, K. L. Liu, Y. M. Dong, X. M. Wu, Z. J. Li and C. Zhang, *Biosensors & bioelectronics*, 2014, 62, 66-72.
41. Y.-W. Zhang, R. Si, C.-S. Liao, C.-H. Yan, C.-X. Xiao and Y. Kou, *The Journal of Physical Chemistry B*, 2003, 107, 10159-10167.